

# Resonant tunneling diode nano-optoelectronic excitable nodes for neuromorphic spike-based information processing

Matěj Hejda,<sup>1</sup> Juan Arturo Alanis,<sup>1</sup> Ignacio Ortega-Piwonka,<sup>2</sup> João Lourenço,<sup>3</sup>  
José Figueiredo,<sup>3</sup> Julien Javaloyes,<sup>2</sup> Bruno Romeira,<sup>4</sup> and Antonio Hurtado<sup>5</sup>

<sup>1</sup>*Institute of Photonics, SUPA Dept of Physics, University of Strathclyde, Glasgow, United Kingdom*

<sup>2</sup>*Dept de Física and IAC-3, Universitat de les Illes Balears, Palma de Mallorca, Spain*

<sup>3</sup>*Centra-Ciências and Departamento de Física, Faculdade de Ciências, Universidade de Lisboa, Lisboa, Portugal*

<sup>4</sup>*Ultrafast Bio and Nanophotonics Group, International Iberian Nanotechnology Laboratory, Braga, Portugal*

<sup>5</sup>*Institute of Photonics, SUPA Department of Physics,*

*University of Strathclyde, Glasgow, United Kingdom*

(Dated: January 31, 2022)

In this work, we introduce an interconnected nano-optoelectronic spiking artificial neuron emitter-receiver system capable of operating at ultrafast rates ( $\sim 100$  ps/optical spike) and with low energy consumption ( $< \text{pJ/spike}$ ). The proposed system combines an excitable resonant tunneling diode (RTD) element exhibiting negative differential conductance, coupled to a nanoscale light source (forming a master node) or a photodetector (forming a receiver node). We study numerically the spiking dynamical responses and information propagation functionality of an interconnected master-receiver RTD node system. Using the key functionality of pulse thresholding and integration, we utilize a single node to classify sequential pulse patterns and perform convolutional functionality for image feature (edge) recognition. We also demonstrate an optically-interconnected spiking neural network model for processing of spatiotemporal data at over 10 Gbps with high inference accuracy. Finally, we demonstrate an off-chip supervised learning approach utilizing spike-timing dependent plasticity for the RTD-enabled photonic spiking neural network. These results demonstrate the potential and viability of RTD spiking nodes for low footprint, low energy, high-speed optoelectronic realization of spike-based neuromorphic hardware.

## I. INTRODUCTION

With the magnitude of data production increasing exponentially, machine learning (ML) approaches and the field of artificial intelligence (AI) have been undergoing a booming development, rapidly becoming ubiquitous in all domains of human endeavour. These methods have allowed machines to gain human-like information processing capabilities (e.g. learning, computer vision, natural language processing (NLP) or complex pattern recognition) and to solve significant computational problems [1]. While AI algorithms achieve new breakthroughs, the hardware used to run those receives in turn less attention. Nowadays, large scale ML models are typically trained on cloud-based computing clusters, with some estimates placing the training energy consumption for a state-of-the-art NLP model on par with six years of total power energy consumption of a human brain [2]. Driven by the goal of reducing energy consumption as well as by the plateauing of empirical chip scaling laws, there has recently been significant growth of interest in non-conventional computing approaches. Neuromorphic (brain-like) engineering develops computer hardware architectures inspired by the brain and by the behaviour of biological neurons. Neuromorphic systems can be operated at various degrees of biological plausibility, directly mapping conventional artificial neural network algorithms onto hardware or capitalising on the rich dynamical behaviour of biological neurons for information processing. While there already are powerful neuromorphic systems based on electronics [3, 4], the reliance on

CMOS technology imposes limits in terms of interconnectivity and component density, with dozens of transistors required per neuron and additional external memories needed for synaptic weights. This results in several  $\mu\text{m}$  large neurons. Since dedicated wiring for every synaptic link is not practical, neuromorphic electronic systems usually employ a shared digital communication bus with time-division multiplexing [5], gaining interconnectivity at the expense of bandwidth, or use schemes such as address-event representation (AER) [6]. As an alternative, hardware technologies relying on physics for neuromorphic computation are nowadays gaining increasing research interest. These include hybrid CMOS/memristive systems (see [2] for an overview), spintronics [7] and photonic systems [8, 9].

Neuromorphic photonics is a nascent field, recently gaining significant traction due to increasing importance of AI algorithms and rapid advances in the field of photonic integrated circuits (PICs). Optoelectronic systems in particular are considered as highly suitable for future cognitive computing hardware, as they benefit from operation with both electrons and photons, each excelling at different key functionalities [14]. Thanks to their capability to address bandwidth and interconnect energy limits in a scalable fashion, optoelectronic systems might prove as the optimal solution to overcome these limitations [15]. There are many different approaches to realization of artificial neural networks in optics (see for example review [16]). Using delayed feedback, recurrent neural networks can be realized in a photonic reservoir computer, yielding networks with large number of virtual

TABLE I. Comparison of photonic and optoelectronic technologies capable of spike (pulse) based signalling.

Photonic platform	Energy/event	Spike event timescales
superconducting Josephson junctions (cryogenic) [10]	$> 2 \cdot 10^{-14}$ J	$> 1$ ns (nTron switching)
phase change material cells [11]	$\sim 10^{-12}$ J	$\sim 500$ ps – 1.5 ns (read/write)
micropillars [12]	$\sim 5 \cdot 10^{-14}$ J (excl. pump)	$\sim 200$ ps
graphene-SA laser [13]	$\sim 10^{-8}$ J	$\sim 20$ $\mu$ s
RTD optoelectronic node [this work]	$\sim 10^{-13}$ J	$\sim 100$ ps

nodes while only requiring very low hardware complexity [17]. Closer to the usual digital implementation of artificial neural networks are platforms that enable accelerated matrix/tensor-based computation [18, 19]. Some photonic systems, such as diffractive surfaces [20, 21], may allow for passive computation by interaction between light and matter. One of the key principles when designing biologically-plausible neuromorphic hardware is excitability and event-based signalling. Biological neurons communicate with electronic signals using a sparse encoding scheme known as *spiking*. Photonic spike-based neuromorphic systems include phase-change material (PCM) based integrated networks of micro-ring resonators [11, 22], photonic crystals [23], superconducting Josephson junctions [10], micropillar lasers [24], excitable semiconductor lasers, including a graphene laser with saturable absorber [25], quantum-dot laser [26–28], micro-ring resonators [29], vertical cavity surface emitting lasers (VCSELs) [30–32] and multi-section VCSELs with saturable absorber [33, 34]. Table I provides comparison of some of these approaches. This wide array of investigated technologies demonstrates the power and high potential of photonics for unconventional brain-inspired computing. Despite the impressive progress, the development of a single, miniaturized light-emitting nanoscale source and detector for spike-based operation (which is key for spike-based, neuromorphic computing in the optoelectronic domain) remains an ongoing, significant challenge.

## II. SPIKING NEUROMORPHIC

### RTD-POWERED OPTOELECTRONIC NODES

In this work, we introduce an optoelectronic spike-based neuromorphic system utilizing a resonant tunneling diode (RTD) element based on a double barrier quantum well (DBQW) epi-layer structure. The DBQW consists of a narrow bandgap semiconductor layer embedded between two thin layers with a wider bandgap (Fig. 1d, inset), with typical barrier thicknesses ranging from 4 to 8 nm, and 1 nm to 3 nm, respectively. Under applied voltage, the structure works as a filter for the carrier’s energy, leading to high carriers’ transmission when energy of the electrons (Fermi sea) resonates with the confinement energy levels of the DBQW. The voltage-controlled probability for incident electrons to cross the barrier is locally maximized, which results in the typical N-shaped voltage-current relation  $f(V)$  with one or more regions

of negative differential conductance (NDC) in between two or more regions of positive differential conductance (PDC) [36] as shown in Fig. 1d. The presence of the non-linearity and gain in the NDC region, persisting from DC up to THz frequencies [37], makes RTDs particularly suitable for high frequency oscillators [38]. This nonlinearity is key for operation of the proposed spiking neuromorphic RTD node as a fast, excitable spiking nonlinear source [39] with intrinsic electrical gain. Previous works have investigated triggering of stochastic excitable responses in hybrid integrated optoelectronic RTD circuits [40, 41] and operation of RTDs with delayed feedback [42], addressing only operation of a single (solitary) device. In this work, we investigate interconnected systems consisting of multiple independent RTD-based monolithic integrated optoelectronic nodes. We employ the nodes as stateless excitable devices and take advantage of the spike-based signalling to implement information processing tasks and multi-device networks with prospects for very low footprint, low energy and high-speed operation due to the use of sub- $\lambda$  elements. We utilize two types of nodes: an electronic-optical (E/O) RTD-LD system, realized with a RTD element coupled to a nanoscale laser diode (LD), and an optical-electronic (O/E) RTD-PD system, realized with a photodiode (PD) coupled to a RTD element. In both node types, spiking threshold can be adjusted via bias voltage tuning. An illustration of two nodes with an unidirectional optical weighted link, representing two feedforward linked neurons, is depicted in Fig. 1a.

#### A. Optoelectronic RTD-system architecture

In both the RTD-LD and RTD-PD nodes, the two functional blocks are integrated in a monolithic, metal dielectric cavity micro-pillar with DBQW regions on GaAs/AlGaAs materials [43] for operation at the wavelength of 850 nm and InP materials [44] for operation at 1550 nm. For simplicity, in this work we focus on one of the two material platforms and investigate InP-based RTD systems throughout our analyses. The micro-pillar is coated by a dielectric cap (typically made of SiO<sub>2</sub>) and metallic layer (typically Au or Ag), similarly to previously reported waveguide-coupled nanoLEDs [45]. A significant advantage of the semiconductor RTD epi-layer design is that it can be used to realize all the required functional blocks of the proposed spiking neuro-

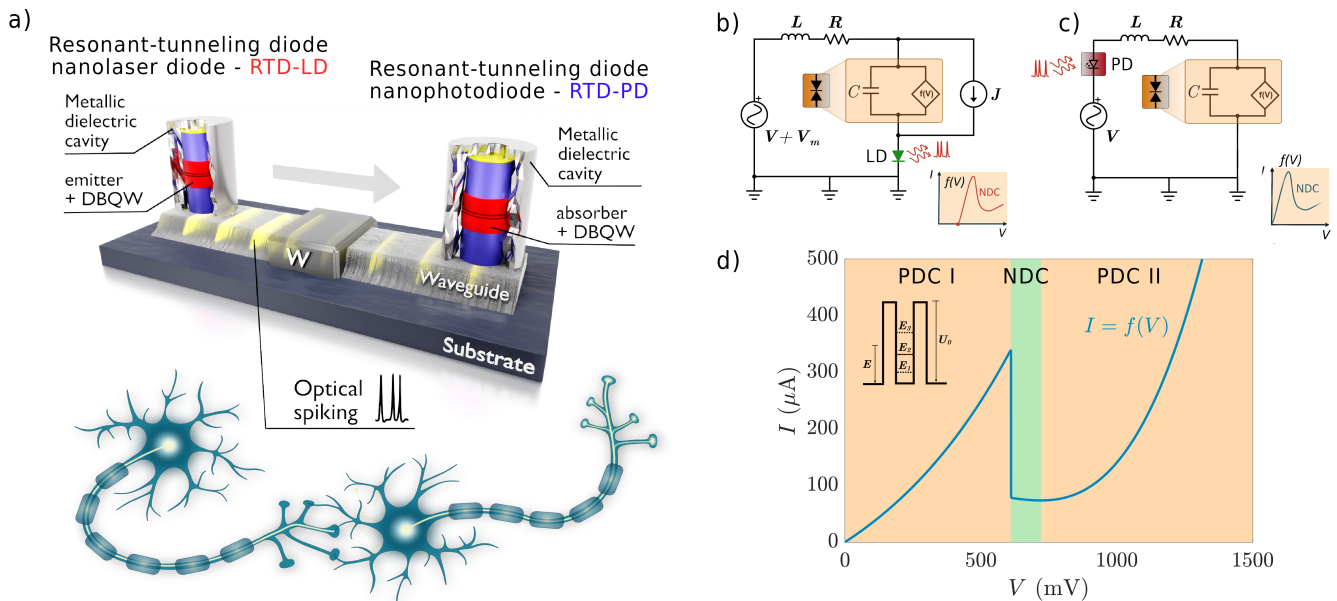


FIG. 1. (a) Illustration of the proposed solution for spike-based neuromorphic system based on two types of RTD-powered optoelectronic nodes: RTD-LD (master) and RTD-PD (receiver) nodes. The RTD-LD and RTD-PD metal-dielectric encapsulated micropillars are coupled using a waveguide with adjustable attenuation factor  $W$ . When subject to external bias, RTD-LD nodes can respond to incoming perturbations with short optical pulses (spikes), which can be processed in the downstream RTD-PD node. This functionality mimics the use of action potential in biological neurons. (b) Lumped circuit scheme for the RTD-LD node. (c) Lumped circuit diagram from the RTD-PD node. (d) The RTD I-V characteristic used in this study, with curve parameters obtained by fitting experimental data (see Supplemental Information [35] for the parameters). Regions of positive differential conductance (PDC) and negative differential conductance (NDC) are highlighted in different colours. The inset shows a simplified DBQW scheme with the discrete energy levels inside the well. Typical thickness of the DBQW region is around 10 nm

165 morphic optoelectronic nodes, including ultra-sensitive  
 166 photodetectors [46, 47], high bandwidth nonlinear be-  
 167 haviour (including spiking responses) in the electric do-  
 168 main, and light emission, including both coherent (laser)  
 169 and non-coherent (light emitting diodes, LEDs) opera-  
 170 tion. This brings the possibility of all-in-one monolithic  
 171 integration of the required functional blocks into singu-  
 172 lar sub-micron scale devices. Specific epi-layer designs  
 173 based upon different materials platforms targeting opera-  
 174 tion at forementioned wavelength ranges, i.e. 1550 nm  
 175 (InP) and 850 nm (GaAs), are currently being investi-  
 176 gated towards the fabrication of the systems proposed in  
 177 this work. For non-coherent signalling between nodes,  
 178 the RTD-LD can also be realized using an RTD-LED  
 179 sub- $\lambda$  element at high (multi-gigahertz) speeds with very  
 180 low power consumption ( $<1$  pJ per emitted spike) [43]. It  
 181 was observed that the light emission efficiency of the pil-  
 182 lar design increases with smaller sizes, with sub-lambda  
 183 pillars yielding very high light-extraction efficiency [48].  
 184 RTD-powered nanolasers and light-sources may also ben-  
 185 efit from their small size in terms of improved operation  
 186 speed and reduced lasing threshold [49]. In a review [2],  
 187 it was stated that a minimum lateral size of hardware  
 188 neurons is to be expected around  $100 \mu\text{m}$ . RTD compo-  
 189 nents, embedded as singular or monolithic sub-micron  
 190 structures, have the potential to be significantly smaller,  
 191 overcoming one of the key expected disadvantages (large

192 footprint) in such systems. Unlike the superconducting  
 193 and fluxonic [50] solutions, the RTD-based optoelectronic  
 194 node can be operated at room temperatures.

195 The synaptic links in this work are required for opti-  
 196 cal signal propagation between nodes and signal weight-  
 197 ing (controllable optical signal attenuation). Recent  
 198 advances in integrated, tuneable waveguide meshes offer  
 199 chip-scale solutions for linear matrix transformations  
 200 [51], which typically underpin the weighting functionali-  
 201 ty in neural networks. The micropillars can be directly  
 202 coupled to waveguides by the means of heterogenous inte-  
 203 gration [52] or coupled together by means of two-photon  
 204 polymerization waveguiding structures [53, 54]. Signal  
 205 attenuation in photonic waveguides can be realized for  
 206 example by the means of balanced Mach-Zehnder inter-  
 207 ferometers, directional couplers [51] or nano-scale phase  
 208 change material (PCM) cells [55]. PCM-based synaptic  
 209 cells also exhibit suitability for fully-optical spike-timing  
 210 based plasticity [56]. The functionality of all-optical  
 211 synaptic signal weighting can also be realized using ver-  
 212 tical cavity semiconductor optical amplifiers (VCSOAs)  
 213 [57] and synaptic interconnections can also be realized  
 214 using integrated optical devices based on photorefractive  
 215 III-V photonic structures on silicon [58].

### III. RTD-LD $\rightarrow$ RTD-PD: THEORY AND DYNAMICS

#### A. Single optoelectronic node

We consider the monolithic nodes as optoelectronic circuits based on an RTD element connected to electrical and/or optical modulation (Fig. 1(b,c)). The circuit dynamics are described by Kirchhoff laws, together with a nanolaser diode model [59–63]:

$$C \frac{dV}{dt} = I - f(V) - \kappa S_m(t) \quad (1)$$

$$L \frac{dI}{dt} = V_m(t) - V - RI \quad (2)$$

$$\frac{dS}{dt} = \left( \gamma_m(N - N_0) - \frac{1}{\tau_p} \right) S + \gamma_m N + \sqrt{\gamma_m N S} \xi(t) \quad (3)$$

$$\frac{dN}{dt} = \frac{J + \eta I}{q_e} - (\gamma_l + \gamma_m + \gamma_{nr})N - \gamma_m(N - N_0)|E|^2 \quad (4)$$

Here,  $V$  is the voltage along the RTD,  $I(t)$  is the circuit's total current,  $S(t)$  is the photon number and  $N(t)$  is the carrier number.  $R$  is the circuit equivalent resistance and  $L$  is the intrinsic inductance of the circuit while  $C$  is the parasitic capacitance of the RTD.  $V_m(t)$  is the modulation voltage function. We consider two node models: a) receiver, an O-E RTD integrated with a photodetector (PD), governed by Eqs. 1-2, which can be driven by external optical pulses (represented as  $S_m(t)$ ) where  $\kappa$  is the photodetector conversion factor translating input optical intensity into a photocurrent [42] signal; b) master, an E-O RTD-LD node, governed by all the shown equations (Eq. 1-4) with omission of the PD term. We assume low input optical power level (with small power variations), allowing for use of linearized sensitivity-power relation in the PD term [47] and static  $f(V)$ . Due to reduced cavity size, the spontaneous and stimulated emission rates are modified as a result of Purcell enhancement of both the radiative processes [59]. For simplicity of analysis, the rate equation model includes only homogeneous broadening effects.  $N_0$  is the transparency carrier number,  $\tau_p$  is the photon lifetime,  $\gamma_m, \gamma_l, \gamma_{nr}$  are respectively the spontaneous emission rate into the lasing mode (where  $\gamma_m \cdot S$  is the stimulated emission rate), radiative decay into the leaky modes and non-radiative spontaneous emission coefficients.  $q_e$  is the electron charge and  $J$  is an input bias current injected into the LD in addition to the RTD current  $I(t)$ . The stochastic nature of the system is given in Eq. 3 by the term  $\gamma_m N$  and the multiplicative noise  $\sqrt{\gamma_m N S} \xi(t)$ , where  $\xi(t)$  is a time-uncorrelated white noise function. The parameters used in this work are available from the Supplemental information [35]. The function  $f(V)$  accounts for the nonlinear relation between the voltage applied across the RTD and the current passing through it. We use an analytical expression for  $f(V)$  derived in [64] and detailed in the Supplemental

Information [35]. The device operates at room temperature (300°K). Fig. 1b shows the experimentally fitted  $f(V)$  characteristic (parameters available from Supplemental information [35]) with a relatively narrow region of negative differential conductance embedded in between two regions of positive differential conductance, labelled as NDC, PDC I and PDC II, respectively. The curve peak is located at  $V = 609.6$  mV, with a local maximal current of  $338.6$   $\mu$ A. At the right of the peak, the current abruptly drops from  $340$   $\mu$ A to  $80$   $\mu$ A in a span of less than  $1$  mV. Further rightwards,  $f(V)$  continues to decrease, although with a much more moderate rate, until it reaches a valley at  $V = 720.7$  mV and a local minimal current of  $73.6$   $\mu$ A. Beyond this point,  $f(V)$  increases again following a diode-like behaviour.

#### B. Dynamical behaviour

When the system (Eqs. 1,2) is biased in the proximity of the peak or valley of its I-V curve and injected with positive or negative voltage pulses respectively, it behaves as an excitable system able to respond with electronic spikes. Using this functionality, numerical simulations of Eqs. (1,2,3,4) are run, where a train of square negative voltage pulses  $V_m$  is used to trigger a spike in the RTD-LD optoelectronic master node (Fig. 2a). Here, the RTD is biased close to the valley point at  $750$  mV. The period of the train is  $2$  ns and each pulse is  $50$  ps long and  $100$  mV deep. No optical modulation is used (i.e.,  $S_m(t) = 0$ ). In total  $50$  simulations are run over  $10$  periods (thus, a total of  $500$  pulses are injected). The RTD responds with upward current pulses (Fig. 2b), each about  $275$  ps long and reaching a peak of  $342$   $\mu$ A. The response delay is roughly  $25$  ps and the rest value of the signal is  $74$   $\mu$ A. Such pulse elicits a weak response when injected into the LD because its peak value only slightly surpasses the LD threshold current for a very brief time. This is why the additional input bias current  $J$  is necessary. When the LD is biased at  $J = 210$   $\mu$ A, the total current injected  $J + I_{mas}(t)$  has a rest value of  $284$   $\mu$ A and a peak value of  $552$   $\mu$ A, well below and well above the threshold current, respectively. In consequence, the LD remains inactive most of the time and emits a pulse in response to each current pulse (Fig. 2c). The optical pulse is shorter, with a duration of  $40$ - $60$  ps (with temporal fluctuations due to the white noise term in Eq. 3) because the LD takes a relatively long time to respond to an above-threshold current while it quickly stops emitting as the current descends under the threshold. This results in the optical pulse being shortened and the response latency increased up to about  $75$  ps. This phenomenon is typical in systems that exhibit transcritical bifurcations and is known as *critical slowing down* [65–68]. The estimate for RTD-LD power consumption is based on the idle state current ( $284$   $\mu$ A), multiplied by the idle voltage bias ( $750$  mV for valley point), resulting in  $213$   $\mu$ W. This is inclusive of the additional  $J$  term that

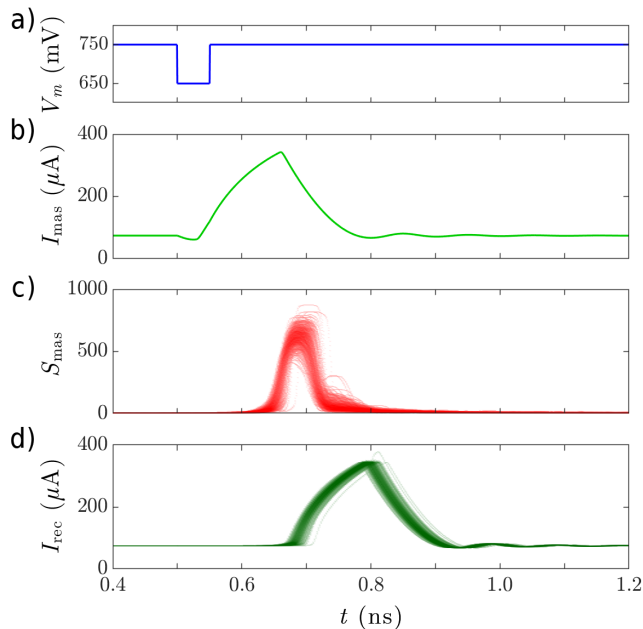


FIG. 2. Steps in 500 responses of the master-receiver optoelectronic system to the same input square pulse. The RTD elements and LDs are biased at  $V_0 = 750$  mV and  $J = 210$   $\mu$ A, respectively. *a*) Square voltage perturbation injected into the master RTD element. *b*) Master RTD electronic pulse response. *c*) Master LD optical pulse response. *d*) Receiver RTD element electronic (current) pulse response.

sets the sub-threshold operation current of the laser. The spiking itself, due to its very short temporal timescales, will require small amount of additional power. Assuming for the spiking event a peak current of 552  $\mu$ A and same voltage value of 750 mV gives a power of 414  $\mu$ W during an approximate time of 100 ps (based on pulse shape from Fig. 2b) with maximum spiking repetition rate interval of approx. 420 ps. Hence, the upper bound on power consumption in the system can be taken as temporally weighted average of the *spike* (100 ps) and *idle* (320 ps) states, resulting in 261  $\mu$ W. Higher firing sparsity (lower spiking rate) with increased inter-spike timing interval will reduce the total power consumption. With upper bound on spike firing repetition rate of 420 ps, the total energy consumption per spike can reach values as low as 110 fJ. We also note that peak and valley voltages in RTDs can be much smaller than 0.5 V, and that RTDs and nanolasers can be designed for operation at lower currents (10  $\mu$ A – 100  $\mu$ A) [69] to further reduce power consumption. In summary, the optoelectronic RTD-LD node has been demonstrated as an excitable system able to generate short optical pulses with low power consumption.

To facilitate networking, the optical pulse leaving the optoelectronic node can be used to drive a second node in a master-receiver layout. With the receiver RTD-PD circuit biased close to the valley of its I-V characteristic ( $V_m(t) = V_0 = 750$  mV), the perturbation  $\kappa S_{mas}(t)$

is able to elicit an excitable response from the receiver RTD in the form of an excitatory current pulse similar to that produced by the master RTD (Fig. 2d), albeit with a fluctuating character. Therefore, the master-receiver integrated circuit is able to propagate (cascade) information by means of optical pulses. The low required values of the  $\kappa$  conversion factor (see Supplemental Information [35]) used in the model demonstrate that cascaded responses require only a small portion of the optical output energy produced by upstream nodes, further increasing the prospects of larger fan-in/fan-outs in networks.

#### IV. INFORMATION PROCESSING WITH RTD-BASED OPTOELECTRONIC NODES

##### A. Single node 8-bit pattern recognition task

Neurons have the ability to integrate a series of input stimuli and elicit a single spike firing response. This happens due to the cumulative effect of separate input perturbations which, when combined, can exceed the neuron firing threshold intensity. A similar integrate and fire (I&F) behaviour can be replicated with RTD devices.

To demonstrate this, we modelled the dynamical response of a single RTD-LD node driven by an AC signal  $V_m$  consisting of short negative sub-threshold square pulses. In this case, the RTD was biased at a voltage  $V_{DC} = 730$  mV ( $I_{DC} = 73$   $\mu$ A), which positions the device's operation point in the valley slightly to the right of the NDC region. The LD was biased at  $J = 210$   $\mu$ A, thus the total current injected ( $J + I_{DC}$ ) has a rest value of 283  $\mu$ A (below the lasing threshold current). For simplicity, we do not include a receiver RTD-PD circuit, but it is assumed that a perturbation  $S_{mas}$  can be propagated to a receiver node in the form of an excitatory current pulse. To show the circuit's I&F functionality, the RTD element was driven by an AC signal consisting of 50 ps pulses of amplitude  $V_{ac} = -15$  mV, separated by 50 ps. Thus, the resulting modulation signal is  $V_m = V_{DC} + V_{ac}$ . Fig. 3a shows the input signal  $V_m$  (top), which consists of three pulse trains with  $\times 6$ ,  $\times 7$  and  $\times 8$  pulses respectively, and the resulting RTD-LD output trace  $S_{mas}$  (bottom). For modulation signals containing  $< 8$  pulses the output remains unperturbed. However, as the number of pulses is increased to 8, their combined effect triggers a firing event in the RTD element, eliciting in turn a spike in the LD output. This I&F behaviour can be exploited to perform an 8-bit pattern recognition task by a single RTD-LD node at very high speed, as is demonstrated in Fig. 3b-d.

In this example, seven different 8-bit patterns, representing Tetris-like blocks, are mapped onto a 4 by 2 grid with individual values of 1 and -1 (representing black and white colour pixels respectively). The corresponding pattern is described by  $V_m$  as a serialized 8-bit signal (top of Fig. 3b). Subsequently, each pattern is multiplied offline by an array of weights  $W$  associated to a

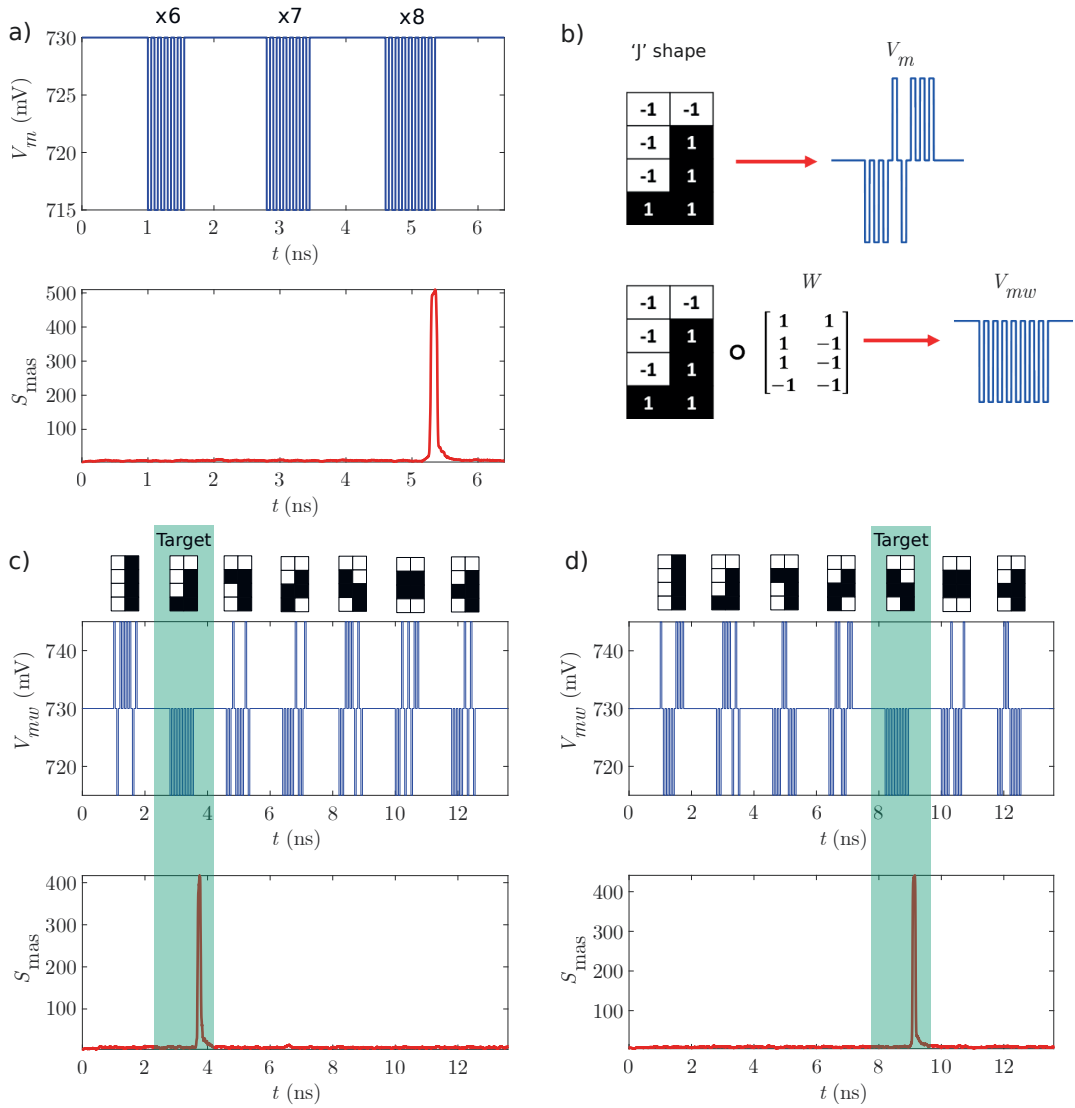


FIG. 3. *a*) RTD-LD response to an AC modulation signal containing three sets of negative square signals with 6, 7 and 8 negative pulses respectively (top) and the corresponding LD output trace (bottom). *b*) Example of a Tetris  $J$ -block represented by a  $4 \times 2$  grid and corresponding serialized signal  $V_m$  (top). The  $J$ -block is weighted offline by element-wise multiplication with a matrix  $W$  converting  $V_m$  to  $V_{mw}$  (bottom). *c*-*d*) Simulation of pattern recognition tasks, where  $W$  was chosen to target the  $J$  *c*) and  $S$ -block *d*) respectively. The corresponding driving signal  $V_{mw}$  is shown (top) accompanied by the LD output trace (bottom). The LD outputs have been smoothed by taking a moving average  $t_{MA} = 0.1$  ns to approximate the effect of the response time of the photodetector and to ease the visualization.

393 target Tetris piece. In the example shown in Fig. 3b, the  
 394 element-wise multiplication between the  $J$ -block pattern  
 395 and  $W = [-1, -1, -1, 1, -1, 1, 1, 1]$  converts the input to  
 396 a serialized all-negative 8-bit signal  $V_{mw}$ . For the simu-  
 397 lation,  $V_{mw}$  included 7 patterns separated by 1 ns. Each  
 398 bit had an activation time of 50 ps with an amplitude  
 399  $V_{ac} = \pm 15$  mV, separated by 50 ps. Two examples of  
 400 a weighted modulation signal  $V_{mw}$ , used to recognise a  
 401  $J$ -shaped and  $S$ -shaped target piece respectively, along  
 402 with their corresponding LD ( $S_{mas}$ ) output traces, are  
 403 shown in Fig. 3c-d. As highlighted by the shaded green  
 404 boxes, the RTD-powered node is able to successfully inte-  
 405 grate 8 pulses (bits) and fire optical spike; thus being

406 able to recognise the desired target piece in each case.

## 407 B. Image edge detection task using sub-threshold 408 pulse integration

409 We further demonstrate the possibility of using a single  
 410 RTD-LD node to perform image edge detection. For this  
 411 task, we utilized a binary image  $M$  of size  $n \times n$  (Fig.  
 412 4a), where black and white pixels are assigned values  
 413 of 1 or -1 respectively. In the pre-processing phase, an  
 414 element-wise product between a  $3 \times 3$  matrix kernel  $K$   
 415 and sections of the binary image  $M_h$  is performed offline:



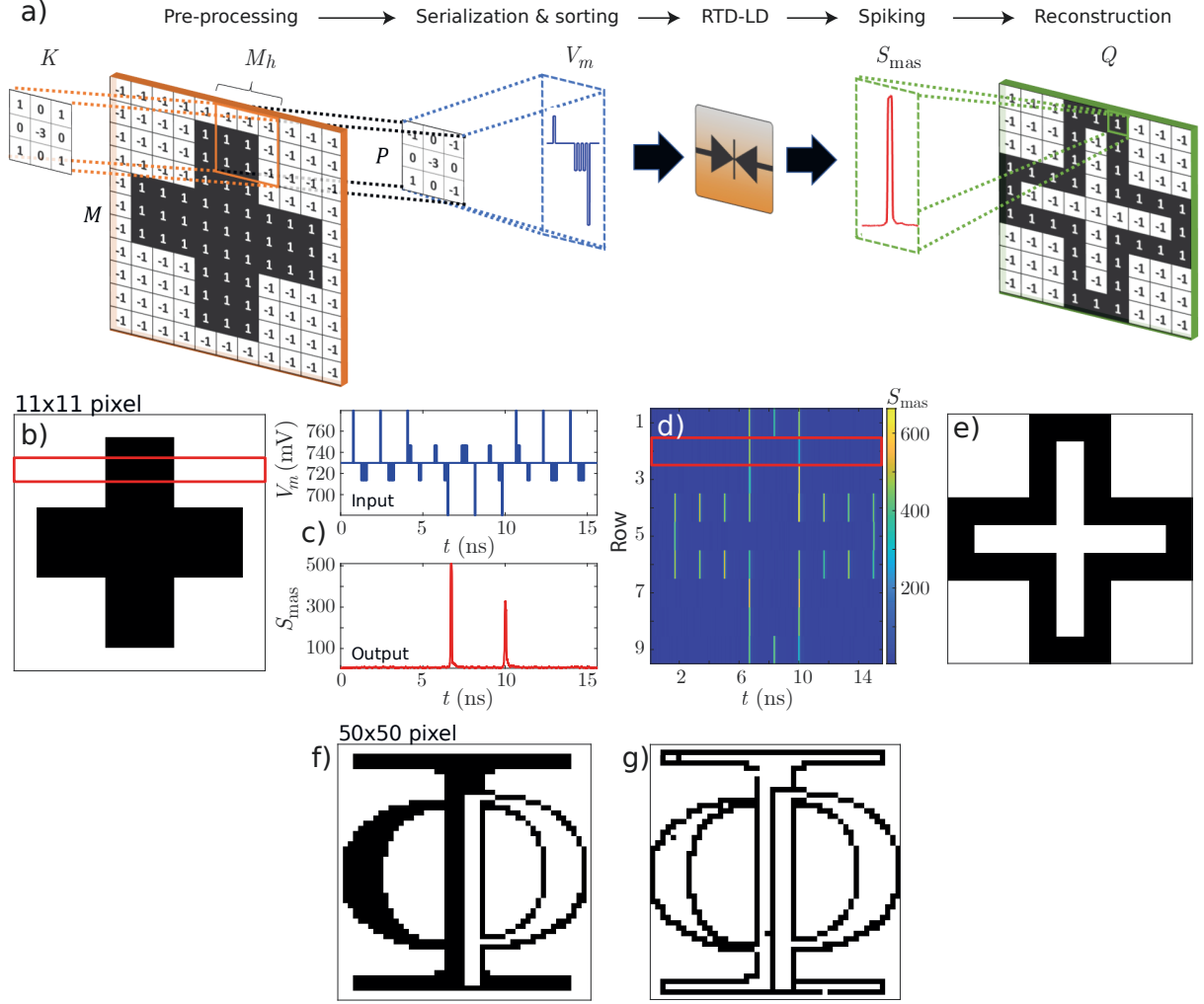


FIG. 4. *a)* Steps followed to perform an edge detection task by a RTD-LD device. The process consists of four main steps: offline multiplication of a binary image  $M$  and kernel  $K$ , serialization and sorting of the 9-bit pattern to generate a modulation signal  $V_m$ , simulation of RTD-LD response to  $V_m$ , and reconstruction of the LD output to a binary image  $Q$ . *b)*  $11 \times 11$  pixels binary image used for edge detection task, where pixels are assigned values of 1 (black) or -1 (white). *c)* Example of modulation signal used as input to drive the RTD (top) and corresponding LD output trace (bottom). *d)* Colour plot showing the complete LD output series used for edge detection of  $M$  (The red box corresponds to the  $S_{mas}$  output plot shown in *c*). *e)* Reconstruction of the LD output trace into a binary image  $Q$ . *f)*  $50 \times 50$  pixel binary image of Strathclyde's Institute of Photonics (IoP) logo. *g)* Reconstructed image after single RTD-LD edge detection task.

$$\begin{aligned}
 P &= K \circ M_h \\
 &= \begin{bmatrix} 1 & 0 & 1 \\ 0 & -3 & 0 \\ 1 & 0 & 1 \end{bmatrix} \circ \begin{bmatrix} M_{i,j} & M_{i,j+1} & M_{i,j+2} \\ M_{i+1,j} & M_{i+1,j+1} & M_{i+1,j+2} \\ M_{i+2,j} & M_{i+2,j+1} & M_{i+2,j+2} \end{bmatrix} \quad (5)
 \end{aligned}$$

where  $i$  and  $j$  are the indices of the individual pixels in  $M_h$ . The resulting matrix  $P$  is serialized as a 9-bit pattern, where each bit is assigned a 50 ps activation pulse and a 50 ps separation for a total of 100 ps per bit. Each pulse is assigned an amplitude  $V_{ac} = \pm 16$  mV  $*P_{k,l}$ , where  $k$  and  $l$  are the indices of individual matrix elements in  $P$ . The serialized bits are sorted such that

their amplitude is rearranged in descending order. This ensures all negative pulses are integrated consecutively to elicit a firing response. The resulting 9-bit modulation signal ( $V_m$ ) is used as the electrical input for the RTD-LD node. The process described above is repeated for each row of  $M$ , taking steps of 1 pixel. Finally, the output of the RTD-LD device is used to reconstruct a binary image  $Q$ , where pixels are assigned a value of 1 when the laser output trace exhibits a spike and -1 otherwise.

An example of an  $11 \times 11$  binary image, used to demonstrate edge detection operation, is shown in Fig. 4b. Each row of  $M$  is described by a modulation signal  $V_m$ , like shown in the top of Fig. 4c, consisting of 9 patterns with a duration of  $100 \times 9$  ps each and temporally

437 separated by 750 ps to account for the time required for  
 438 the LD output to return to zero. For the simulation the  
 439 RTD was biased at the valley  $V_{DC} = 730$  mV. The cor-  
 440 responding  $S_{mas}$  time trace, displayed in the bottom of  
 441 Fig. 4c, shows two spikes of the LD output (pixels 4 and  
 442 6) as a result of the I&F response of the RTD (red box in  
 443 Fig. 4b,d). Fig. 4d shows a colour plot of the LD output  
 444 traces for each row of  $M$ , where the high values of  $S_{mas}$   
 445 correspond to a detected edge. A binary image  $Q$ , recon-  
 446 structed from the RTD-LD output, is shown in Fig. 4e.  
 447 It can be observed that, following an offline element-wise  
 448 multiplication operation with a single 3 by 3 kernel, the  
 449 RTD-LD node is able to consistently detect all edges of  
 450  $M$ , regardless of their orientation. We further show the  
 451 capability of an RTD-LD to consistently detect all edge  
 452 features, by using a  $50 \times 50$  pixels binary image of the  
 453 logo of the Institute of Photonics (IoP) at the Univer-  
 454 sity of Strathclyde (Fig. 4f). The reconstructed image  
 455 in Fig. 4g shows that the RTD-LD node is able to de-  
 456 tect all edges with a 99.7% accuracy. This results are a  
 457 good example of functional tasks which can be performed  
 458 by exploiting the I&F response of an RTD-based spiking  
 459 node.

### 460 C. Feedforward network of optoelectronic nodes

461 Since the information processing capability of an arti-  
 462 ficial neural network (ANN) typically grows with increas-  
 463 ing network complexity, demonstrating networking per-  
 464 formance with multiple optoelectronic spiking nodes is of  
 465 key importance. Here, we numerically investigate the op-  
 466 eration of a spiking variation on the single layer, feedfor-  
 467 ward perceptron model with all-to-one layout. Such net-  
 468 work processes input spike-represented data by weighting  
 469 the signal from each upstream node and summing up all  
 470 the weighted inputs on the the downstream node, which  
 471 fires a spike if the weighted input sum exceeds the firing  
 472 threshold. In the demonstrated model, the spatiotemporal  
 473 patterns of input superthreshold stimuli are injected  
 474 into the first layer of neurons (PREs), where each stim-  
 475 uli results in a guaranteed optical spiking outcome from  
 476 the corresponding PRE node. The optical spiking sig-  
 477 nals from the PREs are weighted by attenuating them  
 478 (multiplying their intensity by a given factor  $w_n$  in the  
 479 numerical model). During the network learning phase, a  
 480 guiding signal carries the data labels alongside each pat-  
 481 tern, marking it as wanted (True) or unwanted (False)  
 482 via change in amplitude. The downstream POST neu-  
 483 ron performs the temporal integration of the upstream  
 484 inputs and fires a spike if the voltage of spiking thresh-  
 485 old is surpassed (integrate & fire operation). A diagram  
 486 of the network is depicted in Fig. 5a, showing how dif-  
 487 ferent patterns (consisting of spikes, in blue) may result  
 488 in activation of spikes and illustrating the dependence of  
 489 weights on the output of the downstream node.

490 In particular, the investigated network consist of five  
 491 layer 1 RTD-LD nodes (PREs, biased in the valley in

492 PDR II,  $V_{DC} = 770$  mV), whose output optical sig-  
 493 nals are propagated through unidirectional, feedforward  
 494 links (each with weight  $w_i$ ) to a single, layer 2 PD-RTD  
 495 (POST) node biased in the valley (in PDR II). In the PD-  
 496 RTD, the PD is current-coupled into the spiking RTD  
 497 element (with the PD conversion factor  $\kappa$ ), directly con-  
 498 verting the incoming optical intensity into the electrical  
 499 domain and resulting in activation of an electronic spik-  
 500 ing signal. In the PREs, we utilize superthreshold input  
 501 trigger pulses of length  $t_{pulse} = 80$  ps, resulting in excita-  
 502 tory (increasing intensity) optical pulses. Since the out-  
 503 put current of a PD at a given time directly depends on  
 504 the input light intensity and temporal distance from pre-  
 505 vious optical spikes, only certain weighted pulse patterns  
 506 may result in sufficiently strong current modulation, ac-  
 507 tivating a spike in the downstream node. That is the  
 508 working principle of the network model for input spa-  
 509 tiotemporal spike-pattern recognition. Visualization of  
 510 the pattern recognition in the network is shown in Fig.  
 511 5b. In this network, the temporal separation between  
 512 each 5-bit input pattern is set to 420 ps, corresponding  
 513 to full network processing capacity of 11.9 Gbps.

### 514 D. Networks: supervised learning method for 515 spatiotemporal pattern recognition

516 Training algorithms are fundamental for useful uti-  
 517 lization of artificial neural networks (ANNs). However,  
 518 training methods for spiking neural networks (SNNs) dif-  
 519 fer from those used for conventional ANNs, which are  
 520 typically based on backpropagation [6]. SNNs can be  
 521 trained using either biologically-plausible local learning  
 522 rules (e.g. spike-timing dependent plasticity (STDP),  
 523 long-term potentiation) or using other specially de-  
 524 signed algorithms such as ReSuMe [70], Resilient-Back-  
 525 propagation (RProp) inspired supervised learning [71]  
 526 and SuperSpike [72], among others. In this work, we in-  
 527 troduce an offline supervised learning rule, following the  
 528 approach introduced in [73] for training memristor-based  
 529 neural networks. However, in contrast to [73], our system  
 530 propagates information using optical spike trains, allow-  
 531 ing us to fully benefit from the advantages of optical sig-  
 532 nalling (e.g. high-bandwidth, low loss waveguiding, non-  
 533 interacting signals etc). Data processing in our network  
 534 follows the two typical phases: a) *training* phase and  
 535 b) *inference* phase. During the training phase, labelled  
 536 patterns are processed by the network. By comparing  
 537 the output state of the network with the label, accord-  
 538 ing adjustments are made to the network weight matrix.  
 539 The learning phase consists of multiple epochs, and pro-  
 540 gresses until the weights stabilize. During a single epoch,  
 541 the dynamical evolution of all the RTD-based nodes in  
 542 the network is numerically evaluated. The use of teacher  
 543 signals (which carry the label of the pattern) allows for  
 544 processing of multiple patterns in a single epoch. In the  
 545 learning phase, three independent patterns are processed  
 546 per single epoch of  $t = 5$  ns.



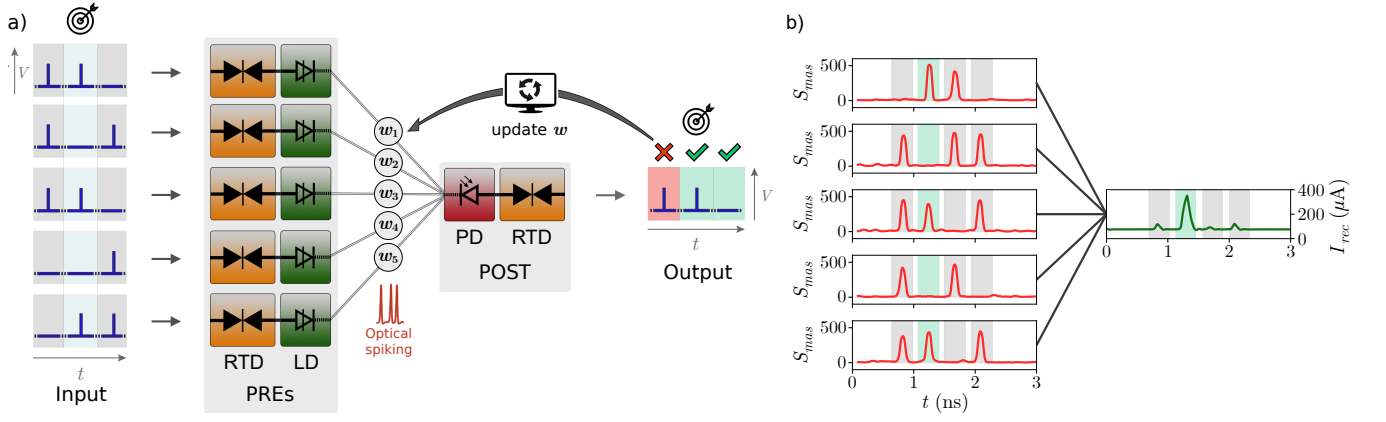


FIG. 5. *a)* Network architecture diagram, illustrating how patterns of input electronic pulses (in blue) enter the RTD-LD nodes and are propagated as optical signals to the downstream node using weighted connection. The output state of the downstream node is compared to the label, and if there is a mismatch between label and output state, the weights are updated. Desired pattern is highlighted with the target icon. *b)* Visualization of inference in 5-to-1 feedforward network numerical model. The guiding signals representing pattern labels are visualized as background shading (green for 'True', grey for 'False'). Only a particular spatial pattern ([1 0 1 0 1], green) results in firing of electric spike of the downstream RTD-PD node (green current trace). The red timetrace represents a simple moving average of the LD output optical signal over  $t_{MA} = 100$  ps.

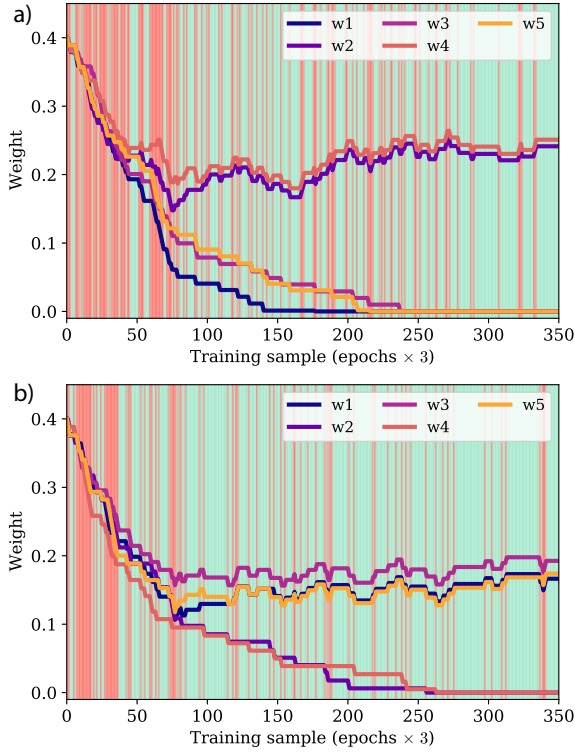


FIG. 6. Demonstration of the supervised learning process for two different spatial patterns with varying number of active bits: *a)* [0 1 0 1 0] and *b)* [1 0 1 0 1]. As the system is used to process to labelled patterns in each epoch, the weights are adjusted using the local learning rule, strengthening connections which produced false negative results and weakening links which produced false positive results. The background colour shows network state (True/False) during each step.

547 Fig. 6 shows the learning process. The target input is a  
 548 5-bit spatial pattern, either [0 1 0 1 0] (Fig. 6a) or [1 0 1 0  
 549 1] (Fig. 6b), and the network is initiated with all weights  
 550 set to an initial value  $w = 0.4$ . We want to note here  
 551 that the weights depend on the current conversion factor  
 552  $\kappa$  of the PD, which was selected in this demonstration  
 553 to bound the weights in the usual interval [0,1]. During  
 554 each learning epoch, three random patterns are picked,  
 555 with a probability  $P_t = 0.25$  of picking the target and  
 556  $P_f = 0.75$  of picking any other pattern. Fig. 6 shows the  
 557 evolution of the weights during each learning step. Green  
 558 background represents *True positive*, *True negative* out-  
 559 comes while red represents *False positive*, *False negative*  
 560 outcomes. For either *True* output state, no weights are  
 561 adjusted during the learning step. For the *False positive*  
 562 output state, the weights that contributed to the firing  
 563 are weakened, with  $\Delta w$  being a function of PRE-POST  
 564 spike separation. The closer the PRE node's spike was  
 565 to activation of a *False positive* POST spike, the higher  
 566 is the depotentiation (weakening) effect. This is a super-  
 567 vised variation on the STDP learning protocol, a specific  
 568 kind of Hebbian learning approach which is believed to  
 569 constitute part of the learning process in biological neural  
 570 networks. A simple rational function was selected for  
 571 the weight adjustment:

$$\Delta w_n = \frac{a}{b \cdot |\Delta T_n| + c} + d \quad (6)$$

572 where

$$\Delta T_n = T_{POST} - T_{PRE,n} \quad (7)$$

573 represents the time interval between the spikes from the  
 574 POST and the PRE neuron  $n$ ,  $a = 9.35 \cdot 10^{-3}$ ,  $b = 5 \cdot 10^9$ ,  
 575  $c = 0.8$ ,  $d = 1.5 \cdot 10^{-3}$ . The numerical coefficients in the

576 rational function were selected based on observed dis-  
 577 tances between spikes in PRE-POST neurons and the  
 578 corresponding desired weight adjustments. Weight ad-  
 579 justment factors as a function of spike separation time  
 580 can be seen in Fig. 7.

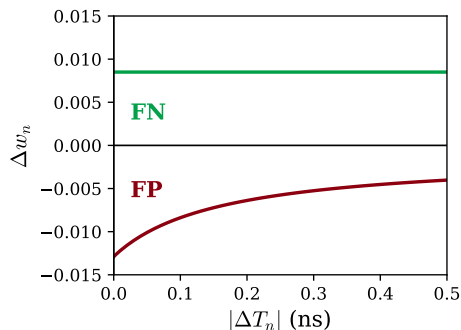


FIG. 7. Weight adjustment factor  $\Delta w_n$  as a function of POST-PRE spiking interval  $|\Delta T_n|$ . For false negatives (FN, in green), the weight adjustment is a constant fixed value. For false positives, the weight adjustment magnitude is a function of  $|\Delta T_n|$ , with closer spikes yielding stronger depotentiation.

581 As the training process proceeds, the occurrence of  
 582 false outcomes gets more and more rare. For both tested  
 583 patterns, the system reaches a stable weight setting in  
 584 approximately 300 patterns (100 epochs). This network  
 585 implementation utilizes only positive weight values, mak-  
 586 ing the solution physically feasible. After the training  
 587 phase, the network can perform inference for recognition  
 588 of the selected spatiotemporal 5-bit pattern. We tested  
 589 all patterns with equal number of active bits against a  
 590 single desired target pattern:  $[0\ 1\ 0\ 1\ 0]$  in one measure-  
 591 ment, and  $[1\ 0\ 1\ 0\ 1]$  in the other. When testing inference  
 592 accuracy for  $[0\ 1\ 0\ 1\ 0]$  against all patterns with  $n_{ON} = 2$   
 593 active bits, the total True response accuracy (with 540  
 594 inferred patterns) was 97.4%. Inferring the pattern  $[1$   
 595  $0\ 1\ 0\ 1]$  against all patterns with same number of ON  
 596 bits ( $n_{ON} = 3$ ) in 540 inference steps yields total True  
 597 response accuracy of 94.8%. The confusion matrices for  
 598 both of these inference procedures are shown in Fig. 8.

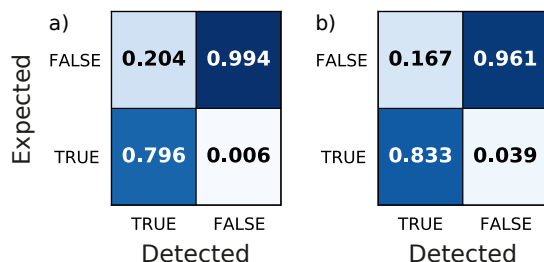


FIG. 8. Confusion matrices for *a)* for inference of pattern  $[0\ 1\ 0\ 1\ 0]$  against all other patterns with two ON bits ( $n = 10$  different patterns, 540 total inference steps); *b)* for inference of pattern  $[1\ 0\ 1\ 0\ 1]$  against all other patterns with three ON bits ( $n = 10$  different patterns, 540 total inference steps).

## V. CONCLUSIONS

600 In this work, we introduce a spiking, nano-  
 601 optoelectronic neuromorphic node based on a DBQW-  
 602 based resonant tunneling diode exhibiting regions of neg-  
 603 ative differential conductance (NDC), enabling neuron-  
 604 like electronic spiking responses at over GHz rates. The  
 605 nodes consist of highly nonlinear, high bandwidth RTD  
 606 elements coupled to either a photodetector or a nanoscale  
 607 laser to enable the reception and transmission of opti-  
 608 cal spikes, respectively. This architecture offers desir-  
 609 able properties including low footprint, operation with  
 610  $<100$  ps input signals and low energy requirements (op-  
 611 eration with mV trigger pulse amplitudes and energies  
 612 of  $<pJ/spike$ ). We investigate and analyze the dynamical  
 613 behaviour of the proposed spike-based neuromorphic  
 614 optoelectronic system and discuss feasible hardware im-  
 615 plementations of individual nodes as well as architectures  
 616 with nodes in interconnected networks.

617 We also numerically demonstrate functional informa-  
 618 tion processing tasks, including 8-bit pattern recogni-  
 619 tion and image feature (edge) detection at over 10 Gbps  
 620 rates (using 50 ps long input signals). Finally, we demon-  
 621 strate network operation, investigating a 5-to-1 feedfor-  
 622 ward spiking neural network architecture. Using physical  
 623 models for each node, we demonstrate that the numeri-  
 624 cally implemented network can be used to classify spatial  
 625 5-bit pulse patterns encoded in time, and we propose a  
 626 supervised learning scheme that employs a spike-timing  
 627 dependent learning rule. During the inference phase,  
 628 we demonstrate 94%+ accuracy for spatiotemporal pulse  
 629 pattern recognition. These reported results represent a  
 630 comprehensive theoretical demonstration of RTD-based,  
 631 optoelectronic, spike-based information processing and  
 632 deliver successful operation in key tasks (pattern recogni-  
 633 tion, image edge-detection) by utilizing either a single  
 634 device or multiple interconnected devices in the form of  
 635 a photonic spiking neural network.

636 Future work will focus on fabrication and characteri-  
 637 zation of the monolithically co-integrated RTD-PD/LD  
 638 nodes and their implementation into on-chip networks.  
 639 Some of the challenges ahead include the selection and  
 640 implementation of optimal solutions for integrated inter-  
 641 links with controllable attenuation, light coupling and  
 642 fan-in/out. For the desirable operation of on-chip net-  
 643 works with higher number ( $\geq 5$ ) of RTD-based artificial  
 644 optoelectronic neurons, a dedicated electronic biasing cir-  
 645 cuitry will also be required to permit adaptive voltage  
 646 bias tuning for each individual node. The achieved in-  
 647 ference accuracy of  $\sim 94\%$  could be further improved by  
 648 e.g. increasing the number of training process epochs. Sim-  
 649 ultaneously, since more complex and multi-layer artifi-  
 650 cial neural networks typically offer better computational  
 651 capability, recurrent connections and multiple (hidden)  
 652 network layers will also be investigated in the future  
 653 with our RTD-based approach, including extension of the  
 654 presented spike-timing based learning rule towards deep  
 655 spiking networks.

## VI. ACKNOWLEDGEMENTS

The authors acknowledge funding support from the European Commission (Grant No. 828841 ChipAI-H2020-FETOPEN-2018–2020), the UKRI Turing AI Acceleration Fellowships Programme (Grant No. EP/V025198/1), and the Office of Naval Research Global (Grant No. ONRGNICOPN62909-18-1-2027). The authors would like to thank Mr Martin Kořátko for providing the 3D graphical visualization of the system.

## VII. SUPPLEMENTAL INFORMATION

See Supplemental Material [35] at [URL will be inserted by publisher] with additional references [74], [75], [76], [77], [78], [79], [80], [81] for more details on the dynamics of the RTD circuit and for device parameters used in the numerical models.

- 
- [1] E. Callaway, ‘It will change everything’: DeepMind’s AI makes gigantic leap in solving protein structures, *Nature* **588**, 203 (2020).
- [2] D. Marković, A. Mizrahi, D. Querlioz, and J. Grollier, Physics for neuromorphic computing, *Nature Reviews Physics* **2**, 499 (2020).
- [3] M. V. DeBole, R. Appuswamy, P. J. Carlson, A. S. Cassidy, P. Datta, S. K. Esser, G. J. Garreau, K. L. Holland, S. Lekuch, M. Mastro, J. McKinstry, B. Taba, C. di Nolfo, B. Paulovicks, J. Sawada, K. Schleupen, B. G. Shaw, J. L. Klamo, M. D. Flickner, J. V. Arthur, D. S. Modha, A. Amir, F. Akopyan, A. Andreopoulos, W. P. Risk, J. Kusnitz, C. Ortega Otero, and T. K. Nayak, TrueNorth: Accelerating From Zero to 64 Million Neurons in 10 Years, *Computer* **52**, 20 (2019).
- [4] M. Davies, N. Srinivasa, T.-H. Lin, G. Chinya, Y. Cao, S. H. Choday, G. Dimou, P. Joshi, N. Imam, S. Jain, Y. Liao, C.-K. Lin, A. Lines, R. Liu, D. Mathaikutty, S. McCoy, A. Paul, J. Tse, G. Venkataramanan, Y.-H. Weng, A. Wild, Y. Yang, and H. Wang, Loihi: A Neuromorphic Manycore Processor with On-Chip Learning, *IEEE Micro* **38**, 82 (2018).
- [5] P. A. Merolla, J. V. Arthur, R. Alvarez-Icaza, A. S. Cassidy, J. Sawada, F. Akopyan, B. L. Jackson, N. Imam, C. Guo, Y. Nakamura, B. Brezzo, I. Vo, S. K. Esser, R. Appuswamy, B. Taba, A. Amir, M. D. Flickner, W. P. Risk, R. Manohar, and D. S. Modha, A million spiking-neuron integrated circuit with a scalable communication network and interface, *Science* **345**, 668 (2014).
- [6] M. Pfeiffer and T. Pfeil, Deep Learning With Spiking Neurons: Opportunities and Challenges, *Frontiers in Neuroscience* **12**, 10.3389/fnins.2018.00774 (2018).
- [7] J. Grollier, D. Querlioz, K. Y. Camsari, K. Everschor-Sitte, S. Fukami, and M. D. Stiles, Neuromorphic spintronics, *Nature Electronics* **3**, 360 (2020).
- [8] B. J. Shastri, A. N. Tait, T. Ferreira de Lima, W. H. P. Pernice, H. Bhaskaran, D. C. Wright, and P. R. Prucnal, Photonics for artificial intelligence and neuromorphic computing, *Nature Photonics* **15**, 102 (2021).
- [9] F. P. Sunny, E. Taheri, M. Nikdast, and S. Pasricha, A Survey on Silicon Photonics for Deep Learning, *ACM Journal on Emerging Technologies in Computing Systems* **17**, 1 (2021).
- [10] J. M. Shainline, S. M. Buckley, A. N. McCaughan, J. Chiles, A. Jafari-Salim, R. P. Mirin, and S. W. Nam, Circuit designs for superconducting optoelectronic loop neurons, *Journal of Applied Physics* **124**, 152130 (2018).
- [11] I. Chakraborty, G. Saha, A. Sengupta, and K. Roy, Toward Fast Neural Computing using All-Photonic Phase Change Spiking Neurons, *Scientific Reports* **8**, 12980 (2018).
- [12] F. Selmi, R. Braive, G. Beaudoin, I. Sagnes, R. Kuszelewicz, T. Erneux, and S. Barbay, Spike latency and response properties of an excitable micropillar laser, *Physical Review E* **94**, 042219 (2016).
- [13] P. Y. Ma, B. J. Shastri, T. Ferreira de Lima, C. Huang, A. N. Tait, M. A. Nahmias, H.-T. Peng, and P. R. Prucnal, Simultaneous excitatory and inhibitory dynamics in an excitable laser, *Optics Letters* **43**, 3802 (2018).
- [14] J. M. Shainline, The Largest Cognitive Systems Will be Optoelectronic, in *2018 IEEE International Conference on Rebooting Computing (ICRC)* (IEEE, 2018) pp. 1–10.
- [15] D. A. B. Miller, Attojoule Optoelectronics for Low-Energy Information Processing and Communications, *Journal of Lightwave Technology* **35**, 346 (2017).
- [16] L. De Marinis, M. Cococcioni, P. Castoldi, and N. Andriolli, Photonic Neural Networks: A Survey, *IEEE Access* **7**, 175827 (2019).
- [17] J. Bueno, S. Maktoobi, L. Froehly, I. Fischer, M. Jacquot, L. Larger, and D. Brunner, Reinforcement learning in a large-scale photonic recurrent neural network, *Optica* **5**, 756 (2018), arXiv:1711.05133.
- [18] Y. Shen, N. C. Harris, S. Skirlo, M. Prabhu, T. Baehr-Jones, M. Hochberg, X. Sun, S. Zhao, H. Larochelle, D. Englund, and M. Soljačić, Deep learning with coherent nanophotonic circuits, *Nature Photonics* **11**, 441 (2017).
- [19] J. Feldmann, N. Youngblood, M. Karpov, H. Gehring, X. Li, M. Stappers, M. Le Gallo, X. Fu, A. Lukashchuk, A. S. Raja, J. Liu, D. C. Wright, A. Sebastian, T. J. Kippenberg, W. H. P. Pernice, and H. Bhaskaran, Parallel convolutional processing using an integrated photonic tensor core, *Nature* **589**, 52 (2021).
- [20] X. Lin, Y. Rivenson, N. T. Yardimci, M. Veli, Y. Luo, M. Jarrahi, and A. Ozcan, All-optical machine learning using diffractive deep neural networks, *Science* **361**, 1004 (2018).
- [21] Y. Luo, D. Mengu, N. T. Yardimci, Y. Rivenson, M. Veli, M. Jarrahi, and A. Ozcan, Design of task-specific optical systems using broadband diffractive neural networks, *Light: Science & Applications* **8**, 112 (2019).
- [22] J. Feldmann, N. Youngblood, D. C. Wright, H. Bhaskaran, and W. H. P. Pernice, All-optical spiking neurosynaptic networks with self-learning capabilities, *Nature* **569**, 208 (2019).

- [23] F. Laporte, A. Katumba, J. Dambre, and P. Bienstman, Numerical demonstration of neuromorphic computing with photonic crystal cavities, *Optics Express* **26**, 7955 (2018).
- [24] V. A. Pammi, K. Alfaro-Bittner, M. G. Clerc, and S. Barbay, Photonic Computing With Single and Coupled Spiking Micropillar Lasers, *IEEE Journal of Selected Topics in Quantum Electronics* **26**, 1 (2020).
- [25] P. Y. Ma, B. J. Shastri, T. Ferreira de Lima, A. N. Tait, M. A. Nahmias, and P. R. Prucnal, All-optical digital-to-spike conversion using a graphene excitable laser, *Optics Express* **25**, 33504 (2017).
- [26] C. Mesaritakis, A. Kapsalis, A. Bogris, and D. Syvridis, Artificial Neuron Based on Integrated Semiconductor Quantum Dot Mode-Locked Lasers, *Scientific Reports* **6**, 39317 (2016).
- [27] J. Robertson, T. Ackemann, L. F. Lester, and A. Hurtado, Externally-Triggered Activation and Inhibition of Optical Pulsating Regimes in Quantum-Dot Mode-locked Lasers, *Scientific Reports* **8**, 12515 (2018).
- [28] G. Sarantoglou, M. Skontranis, and C. Mesaritakis, All Optical Integrate and Fire Neuromorphic Node Based on Single Section Quantum Dot Laser, *IEEE Journal of Selected Topics in Quantum Electronics* **26**, 1 (2020).
- [29] J. Xiang, A. Torchy, X. Guo, and Y. Su, All-Optical Spiking Neuron Based on Passive Microresonator, *Journal of Lightwave Technology* **38**, 4019 (2020).
- [30] J. Robertson, M. Hejda, J. Bueno, and A. Hurtado, Ultrafast optical integration and pattern classification for neuromorphic photonics based on spiking VCSEL neurons, *Scientific Reports* **10**, 6098 (2020).
- [31] M. Hejda, J. Robertson, J. Bueno, and A. Hurtado, Spike-based information encoding in vertical cavity surface emitting lasers for neuromorphic photonic systems, *Journal of Physics: Photonics* **2**, 044001 (2020).
- [32] M. Hejda, J. Robertson, J. Bueno, J. A. Alanis, and A. Hurtado, Neuromorphic encoding of image pixel data into rate-coded optical spike trains with a photonic VCSEL-neuron, *APL Photonics* **6**, 060802 (2021).
- [33] S. Xiang, Z. Ren, Y. Zhang, X. Guo, Z. Song, A. Wen, and Y. Hao, Hardware Architecture and Algorithm Co-design for Multi-Layer Photonic Neuromorphic Network with Excitable VCSELs-SA, in *Optical Fiber Communication Conference (OFC) 2020* (OSA, Washington, D.C., 2020) p. W3A.1.
- [34] Y. Zhang, S. Xiang, X. Guo, A. Wen, and Y. Hao, The winner-take-all mechanism for all-optical systems of pattern recognition and max-pooling operation, *Journal of Lightwave Technology* , 1 (2020).
- [35] M. Hejda, J. A. Alanis, I. Ortega-Piwonka, J. Lourenço, J. Figueiredo, J. Javaloyes, B. Romeira, and A. Hurtado, Supplementary Information: "Resonant tunneling diode nano-optoelectronic excitable nodes for neuromorphic spike-based information processing" (2022), arXiv:2107.06721.
- [36] J. Wang, A. Al-Khalidi, L. Wang, R. Morariu, A. Ofaire, and E. Wasige, 15-Gb/s 50-cm Wireless Link Using a High-Power Compact III-V 84-GHz Transmitter, *IEEE Transactions on Microwave Theory and Techniques* , 1 (2018).
- [37] R. Izumi, S. Suzuki, and M. Asada, 1.98 THz resonant-tunneling-diode oscillator with reduced conduction loss by thick antenna electrode, in *2017 42nd International Conference on Infrared, Millimeter, and Terahertz Waves (IRMMW-THz)* (IEEE, 2017) pp. 1–2.
- [38] M. Feiginov, Frequency Limitations of Resonant-Tunneling Diodes in Sub-THz and THz Oscillators and Detectors, *Journal of Infrared, Millimeter, and Terahertz Waves* **40**, 365 (2019).
- [39] I. Ortega-Piwonka, O. Piro, J. M. L. Figueiredo, B. Romeira, and J. Javaloyes, Bursting and Excitability in Neuromorphic Resonant Tunneling Diodes, *Physical Review Applied* **15**, 034017 (2021).
- [40] B. Romeira, J. Javaloyes, C. N. Ironside, J. M. L. Figueiredo, S. Balle, and O. Piro, Excitability and optical pulse generation in semiconductor lasers driven by resonant tunneling diode photo-detectors, *Optics Express* **21**, 20931 (2013).
- [41] B. Romeira, R. Avó, J. Javaloyes, S. Balle, C. N. Ironside, and J. M. L. Figueiredo, Stochastic induced dynamics in neuromorphic optoelectronic oscillators, *Optical and Quantum Electronics* **46**, 1391 (2014).
- [42] B. Romeira, J. M. L. Figueiredo, and J. Javaloyes, Delay dynamics of neuromorphic optoelectronic nanoscale resonators: Perspectives and applications, *Chaos: An Interdisciplinary Journal of Nonlinear Science* **27**, 114323 (2017).
- [43] B. Romeira, J. M. L. Figueiredo, and J. Javaloyes, NanoLEDs for energy-efficient and gigahertz-speed spike-based sub- $\lambda$  neuromorphic nanophotonic computing, *Nanophotonics* 10.1515/nanoph-2020-0177 (2020).
- [44] B. Romeira, L. Pessoa, H. Salgado, C. Ironside, and J. M. L. Figueiredo, Photo-Detectors Integrated with Resonant Tunneling Diodes, *Sensors* **13**, 9464 (2013).
- [45] V. Dolores-Calzadilla, B. Romeira, F. Pagliano, S. Birindelli, A. Higuera-Rodriguez, P. J. van Veldhoven, M. K. Smit, A. Fiore, and D. Heiss, Waveguide-coupled nanopillar metal-cavity light-emitting diodes on silicon, *Nature Communications* **8**, 14323 (2017).
- [46] A. Pfenning, F. Hartmann, M. Rebello Sousa Dias, F. Langer, M. Kamp, L. K. Castelano, V. Lopez-Richard, G. E. Marques, S. Höfling, and L. Worschech, Photocurrent-voltage relation of resonant tunneling diode photodetectors, *Applied Physics Letters* **107**, 081104 (2015).
- [47] A. Pfenning, F. Hartmann, F. Langer, M. Kamp, S. Höfling, and L. Worschech, Sensitivity of resonant tunneling diode photodetectors, *Nanotechnology* **27**, 355202 (2016).
- [48] B. Romeira, J. Borme, H. Fonseca, J. Gaspar, and J. B. Nieder, Efficient light extraction in subwavelength GaAs/AlGaAs nanopillars for nanoscale light-emitting devices, *Optics Express* **28**, 32302 (2020).
- [49] B. Romeira and A. Fiore, Physical Limits of NanoLEDs and Nanolasers for Optical Communications, *Proceedings of the IEEE* **108**, 735 (2020).
- [50] J. M. Shainline, Fluxonic Processing of Photonic Synapse Events, *IEEE Journal of Selected Topics in Quantum Electronics* **26**, 1 (2020).
- [51] D. Pérez, I. Gasulla, and J. Capmany, Programmable multifunctional integrated nanophotonics, *Nanophotonics* **7**, 1351 (2018).
- [52] D. Jevtics, J. McPhillimy, B. J. E. Guilhabert, J. A. Alanis, H. H. Tan, C. Jagadish, M. D. Dawson, A. Hurtado, P. W. Parkinson, and M. J. Strain, Characterisation, Selection and Micro-Assembly of Nanowire Laser Systems, *Nano Letters* , acs.nanolett.9b05078 (2020).

- [53] C. Maibohm, O. F. Silvestre, J. Borme, M. Sinou, K. Heggarty, and J. B. Nieder, Multi-beam two-photon polymerization for fast large area 3D periodic structure fabrication for bioapplications, *Scientific Reports* **10**, 8740 (2020).
- [54] R. M. R. Adão, B. Romeira, and J. B. Nieder, Design and Fabrication of 3D Interconnects for Photonic Neuronal Networks Using Two-Photon Polymerization, in *Conference on Lasers and Electro-Optics* (OSA, San Jose, California, 2021) p. ATH1R.7.
- [55] A.-K. U. Michel, M. Sousa, M. Yarema, O. Yarema, V. Ovuka, N. Lassaline, V. Wood, and D. J. Norris, Optical Properties of Amorphous and Crystalline GeTe Nanoparticle Thin Films: A Phase-Change Material for Tunable Photonics, *ACS Applied Nano Materials* **3**, 4314 (2020).
- [56] Z. Cheng, C. Ríos, W. H. P. Pernice, C. D. Wright, and H. Bhaskaran, On-chip photonic synapse, *Science Advances* **3**, e1700160 (2017).
- [57] J. A. Alanis, J. Robertson, M. Hejda, and A. Hurtado, Weight Adjustable Photonic Synapse by Non-Linear Gain in a Vertical Cavity Semiconductor Optical Amplifier, *Applied Physics Letters* 10.1063/5.0064374 (2021).
- [58] P. Stark, F. Horst, R. Dangel, J. Weiss, and B. J. Offrein, Opportunities for integrated photonic neural networks, *Nanophotonics* **9**, 4221 (2020).
- [59] B. Romeira and A. Fiore, Purcell effect in the stimulated and spontaneous emission rates of nanoscale semiconductor lasers, *IEEE Journal of Quantum Electronics* **54**, 1 (2018).
- [60] H. Yokoyama and S. D. Brorson, Rate equation analysis of microcavity lasers, *Journal of Applied Physics* **66**, 4801 (1989), <https://doi.org/10.1063/1.343793>.
- [61] J. Mørk and G. L. Lippi, Rate equation description of quantum noise in nanolasers with few emitters, *Applied Physics Letters* **112**, 141103 (2018), <https://doi.org/10.1063/1.5022958>.
- [62] G. Bjork and Y. Yamamoto, Analysis of semiconductor microcavity lasers using rate equations, *IEEE Journal of Quantum Electronics* **27**, 2386 (1991).
- [63] P. R. Rice and H. J. Carmichael, Photon statistics of a cavity-qed laser: A comment on the laser-phase-transition analogy, *Phys. Rev. A* **50**, 4318 (1994).
- [64] J. N. Schulman, H. J. De Los Santos, and D. H. Choi, Physics-based RTD current-voltage equation, *IEEE Electron Device Letters* **17**, 220 (1996).
- [65] J. R. Tredicce, G. L. Lippi, P. Mandel, B. Charasse, A. Chevalier, and B. Picqué, Critical slowing down at a bifurcation, *American Journal of Physics* **72**, 799 (2004), <https://doi.org/10.1119/1.1688783>.
- [66] M. Marconi, C. Métayer, A. Acquaviva, J. M. Boyer, A. Gomel, T. Quiniou, C. Masoller, M. Giudici, and J. R. Tredicce, Testing critical slowing down as a bifurcation indicator in a low-dissipation dynamical system, *Phys. Rev. Lett.* **125**, 134102 (2020).
- [67] W. Scharpf, M. Squicciarini, D. Bromley, C. Green, J. Tredicce, and L. Narducci, Experimental observation of a delayed bifurcation at the threshold of an argon laser, *Optics Communications* **63**, 344 (1987).
- [68] P. Mandel and T. Erneux, Laser Lorenz equations with a time-dependent parameter, *Phys. Rev. Lett.* **53**, 1818 (1984).
- [69] B. Romeira and A. Fiore, Purcell Effect in the Stimulated and Spontaneous Emission Rates of Nanoscale Semiconductor Lasers, *IEEE Journal of Quantum Electronics* **54**, 1 (2018).
- [70] F. Ponulak and A. Kasiński, Supervised Learning in Spiking Neural Networks with ReSuMe: Sequence Learning, Classification, and Spike Shifting, *Neural Computation* **22**, 467 (2010).
- [71] S. McKennoch, D. Liu, and L. G. Bushnell, Fast Modifications of the SpikeProp Algorithm, in *The 2006 IEEE International Joint Conference on Neural Network Proceedings* (IEEE, 2006) pp. 3970–3977.
- [72] F. Zenke and S. Ganguli, SuperSpike: Supervised Learning in Multilayer Spiking Neural Networks, *Neural Computation* **30**, 1514 (2018).
- [73] W. Wang, G. Pedretti, V. Milo, R. Carboni, A. Calderoni, N. Ramaswamy, A. S. Spinelli, and D. Ielmini, Learning of spatiotemporal patterns in a spiking neural network with resistive switching synapses, *Science Advances* **4**, eaat4752 (2018).
- [74] S. Diebold, K. Nishio, Y. Nishida, J. . Kim, K. Tsuruda, T. Mukai, M. Fujita, and T. Nagatsuma, High-speed error-free wireless data transmission using a terahertz resonant tunnelling diode transmitter and receiver, *Electronics Letters* **52**, 1999 (2016).
- [75] A. L. Hodgkin and A. F. Huxley, A quantitative description of membrane current and its application to conduction and excitation in nerve, *The Journal of Physiology* **117**, 500 (1952).
- [76] A. L. Hodgkin, A. F. Huxley, and B. Katz, Measurement of current-voltage relations in the membrane of the giant axon of *Loligo*, *The Journal of Physiology* **116**, 424 (1952).
- [77] L. Kuhnert, K. I. Agladze, and V. I. Krinsky, Image processing using light-sensitive chemical waves., *Nature* **337**, 244 (1989).
- [78] A. Samardak, A. Nogaret, N. Janson, A. Balanov, I. Farrer, and D. Ritchie, Spiking computation and stochastic amplification in a neuron-like semiconductor microstructure, *Journal of Applied Physics* **109** (2011).
- [79] D. Goulding, S. P. Hegarty, O. Rasskazov, S. Melnik, M. Hartnett, G. Greene, J. G. McInerney, D. Rachinskii, and G. Huyet, Excitability in a Quantum Dot Semiconductor Laser with Optical Injection, *Physical Review Letters* **98**, 153903 (2007).
- [80] F. Selmi, R. Braive, G. Beaudoin, I. Sagnes, R. Kuszelewicz, and S. Barbay, Relative Refractory Period in an Excitable Semiconductor Laser, *Physical Review Letters* **112**, 183902 (2014).
- [81] S. Barbay, R. Kuszelewicz, and A. M. Yacomotti, Excitability in a semiconductor laser with saturable absorber, *Optics Letters* **36**, 4476 (2011).